Joule

CellPress

Article

Praseodymium Telluride: A High-Temperature, High-*ZT* Thermoelectric Material

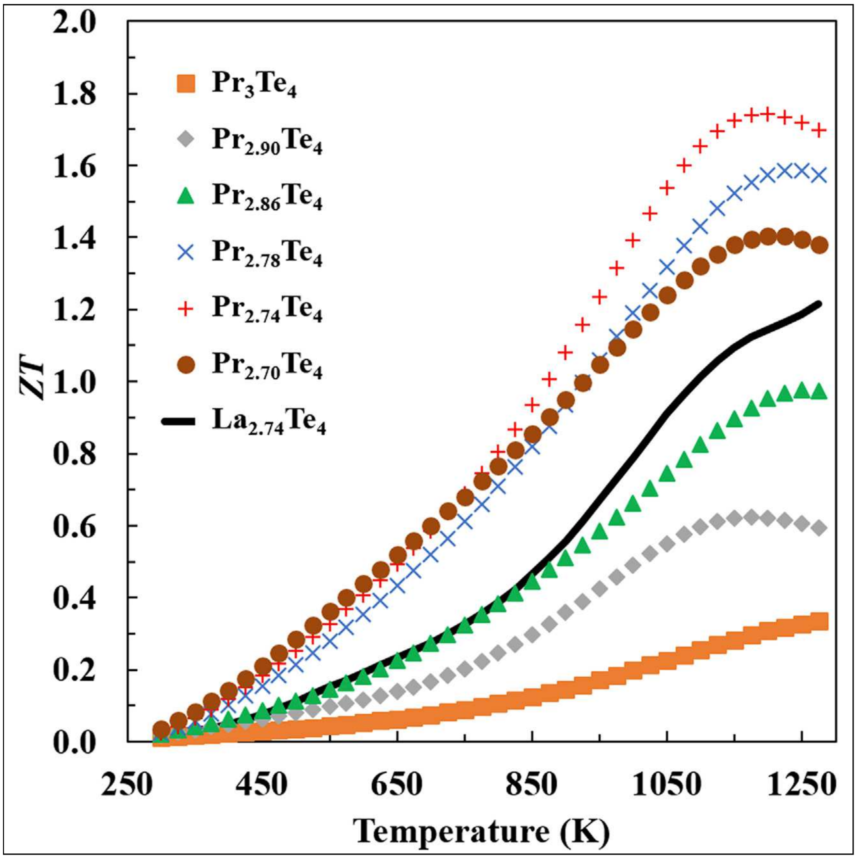

Praseodymium is known to have interesting optical and electronic properties but has been underutilized in the thermoelectric community. We synthesized a series of $Pr_{3-x}Te_4$ compounds and verified their phase purity and composition via Rietveld refinement of X-ray data, wavelength dispersive spectroscopy, and Hall carrier concentration with excellent agreement with the nominal stoichiometry. Measurement of transport properties indicate we were able to achieve a peak *ZT* = 1.7 at 1,200 K, the highest figure of merit reported above 1,000 K.

Dean Cheikh, Brea E. Hogan, Trinh Vo, ..., Bruce S. Dunn, Jean-Pierre Fleurial, Sabah K. Bux

sabah.k.bux@jpl.nasa.gov

HIGHLIGHTS

Praseodymium has been known to have interesting optical and electronic properties

Investigated the effects of *4f* electrons in Pr as a method of improving *ZT*

$Pr_{2.74}Te_4$ possesses a peak *ZT* = 1.7 at 1,200 K, the highest *ZT* reported above 1,000 K

Cheikh et al., Joule 2, 698–709
April 18, 2018 © 2018 Elsevier Inc.
https://doi.org/10.1016/j.joule.2018.01.013

Joule

CellPress

Article

Praseodymium Telluride: A High-Temperature, High-ZT Thermoelectric Material

Dean Cheikh,[1,2] Brea E. Hogan,[2] Trinh Vo,[2] Paul Von Allmen,[2] Kathleen Lee,[2] David M. Smiadak,[3] Alexandra Zevalkink,[3] Bruce S. Dunn,[1] Jean-Pierre Fleurial,[2] and Sabah K. Bux[2,4,*]

SUMMARY

Refractory rare-earth tellurides with the Th_3P_4 structure type have attracted considerable interest as high-performance thermoelectric materials since the 1980s due to their high dimensionless figure of merit (*ZT*). Extensive work has been conducted on $La_{3-x}Te_4$ with peak *ZT* values greater than 1.1 at 1,273 K. The high *ZT* of $La_{3\text{-}x}Te_4$ is in part due to a large peak in the density of states near the Fermi level from the La *5d* states. Here, we revisit $Pr_{3-x}Te_4$, for which our electronic structure calculations predict a favorable modification of the density of states by the introduction of praseodymium's *4f* electrons. This was experimentally verified by preparing $Pr_{3-x}Te_4$ samples with varying Pr vacancy concentrations using a mechanochemical synthesis approach. The thermoelectric properties were measured and a *ZT* of 1.7 at 1,200 K was achieved with $Pr_{2.74}Te_4$. The 50% improvement in peak *ZT* compared with $La_{3-x}Te_4$ resulted from an increased effective mass, improved Seebeck coefficient, and lower thermal conductivity.

INTRODUCTION

Thermoelectric materials have been integrated into solid-state energy conversion devices, which can either function as electrical power generators or be utilized as heat pumps for electronic refrigeration. Si-Ge alloys, PbTe, and Te-Ag-Ge-Sb (TAGS) have been successfully integrated into radioisotope thermoelectric generators (RTGs) to enable deep space and planetary scientific exploration of our solar system for more than 50 years. RTGs have demonstrated long-term reliability and longevity, as evidenced by the *Voyager 1* and *Voyager 2* missions operating continuously for over 40 years.[1]

While systems built using heritage thermoelectric materials have demonstrated high reliability, one limiting factor is the fact that they exhibit modest thermal-to-electric energy conversion efficiency (approximately 6.5% at the system's beginning-of-life, BOL). This is because their average dimensionless figure of merit (*ZT*) values over their operating temperature range are significantly lower than 1 (about 0.80 for PbTe/TAGS materials across a 811–483 K temperature range and 0.55 for Si-Ge alloys over a 1,273–573 K temperature range).[2–5] The dimensionless thermoelectric figure of merit is defined as $ZT = \frac{S^2 T}{\rho \kappa}$, where S is the Seebeck coefficient, T is temperature, ρ is electrical resistivity, and κ is thermal conductivity. Therefore, identifying materials that possess a high Seebeck coefficient, low resistivity, and low thermal conductivity would allow for larger scientific payloads, decrease the amount of radioisotope heat-source fuel used, and reduce the weight of the RTG for a given power level.[6]

Context & Scale

Thermoelectric generators have been an enabling technology for reliably powering many long-lived space science and exploration missions by the National Aeronautics and Space Administration such as the *Voyager* missions and the recent Mars rover, *Curiosity*. A significant increase in conversion efficiency by materials such as $Pr_{3-x}Te_4$ would translate into a reduction in the amount of expensive heat-source fuel and could allow for an increase in the available power as well as more capable payloads for a given mission. Beyond space applications, higher efficiencies would benefit the recent surge of interest in implementing thermoelectrics for terrestrial applications such as waste heat recovery from automobiles and industrial processes.

Lanthanum telluride ($La_{3-x}Te_4$) has been identified as a potential material for high-temperature thermoelectric applications.[3] $La_{3-x}Te_4$ possesses the defect thorium phosphide (Th_3P_4) structure type, with 28 atoms per unit cell, which accommodates vacancies on up to one-ninth of the rare-earth sites. Each La atom donates three electrons and each tellurium atom accepts two electrons, resulting in one free electron per La_3Te_4 formula unit. Therefore, the carrier concentration is tied to the number of La vacancies and the electronic properties can be tuned between metallic behavior when $x = 0$ (La_3Te_4) and semi-insulating when $x = 0.33$ ($La_{2.67}Te_4$). Additionally, $La_{3-x}Te_4$ exhibits a relatively low lattice thermal conductivity resulting from the complexity of the Th_3P_4 structure type, electron-phonon scattering from the high carrier concentration, and phonon scattering from vacancies. As a result, $La_{3-x}Te_4$ has a high peak ZT of 1.1 at 1,273 K for $x = 0.23$.[7]

Other rare-earth tellurides possessing the Th_3P_4 structure type have also been studied for potential use as thermoelectric materials.[4,8–14] This is due to their stability in the high-temperature range of interest for RTGs and the large ZT values exhibited by some of the compounds.[4,15] However, reproducibility of the thermoelectric properties of specific stoichiometry of these compounds has proved challenging. Melt synthesis or solid-state reactions of the elemental species were used extensively in reports examining the rare-earth tellurides.[16–18] These techniques often require high temperatures (>2,000 K) and typically result in inhomogeneous samples. The large difference in melting points between tellurium (722 K) and the rare-earth elements (1,193 K for lanthanum and 1,208 K for praseodymium) leads to vapor-phase loss of tellurium and alters the final stoichiometry of the products, which are very sensitive to stoichiometric deviations due to vacancy doping. Additionally, the oxygen sensitivity of the rare-earth elements and tellurides is problematic, especially at elevated temperatures. Recently it has been demonstrated that mechanochemical synthesis can be used to synthesize $La_{3-x}Te_4$ at low temperatures.[7] The use of mechanochemical synthesis circumvents the challenges associated with high-temperature synthetic techniques by mechanochemically synthesizing $La_{3-x}Te_4$ product in a closed system (ball mill vial) operating at room temperature, thereby allowing samples to be prepared reproducibly with precise stoichiometry and in a short period of time.

The band structure of $La_{3-x}Te_4$ has been shown to be favorable for a large Seebeck coefficient due to heavy conduction bands.[19] The electronic density of states (DOS) in the conduction band of $La_{3-x}Te_4$ is composed almost entirely of La states, while the Te states dominate the valence band.[19,20] A large Seebeck coefficient can be achieved at high carrier concentrations due to a sharp peak in the DOS near the Fermi level in the conduction band. Modifications of the DOS to further improve the Seebeck coefficient have been attempted using divalent substitutions of Ca and Yb on the La site, but were found to have little impact on the thermoelectric properties.[21,22] Examination of the DOS of $La_{3-x}Te_4$ reveals that while the main contribution to the peak in the conduction band comes from the La *5d* orbital, there is also contribution from the *4f* states. The smaller contribution of the *4f* orbitals results from the absence of *f* electrons in La *4f* shell. However, since the *4f* states are located above the Fermi level, an increase in the DOS or sharpening of the peak at the Fermi level by introduction of *4f* electrons could increase the Seebeck coefficient and ultimately the thermoelectric performance of the material.

Previously we have studied the effects of $Ce_{3-x}Te_4$, where Ce possesses 1 electron in the valence shell. We found that the thermoelectric properties of $Ce_{3-x}Te_4$ were similar to that of $La_{3-x}Te_4$[20] (also J.P. Fleurial, personal communication). To investigate the effects of the *4f* electrons on the DOS, we studied $Pr_{3-x}Te_4$, where the Pr

[1]Department of Materials Science and Engineering, University of California, Los Angeles, Los Angeles, CA 90095, USA

[2]Thermal Energy Conversion Research and Advancement Group, Jet Propulsion Laboratory/California Institute of Technology, 4800 Oak Grove Drive, Pasadena, CA 91109, USA

[3]Department of Materials Science and Engineering, Michigan State University, East Lansing, MI 48824, USA

[4]Lead Contact

*Correspondence: sabah.k.bux@jpl.nasa.gov

https://doi.org/10.1016/j.joule.2018.01.013

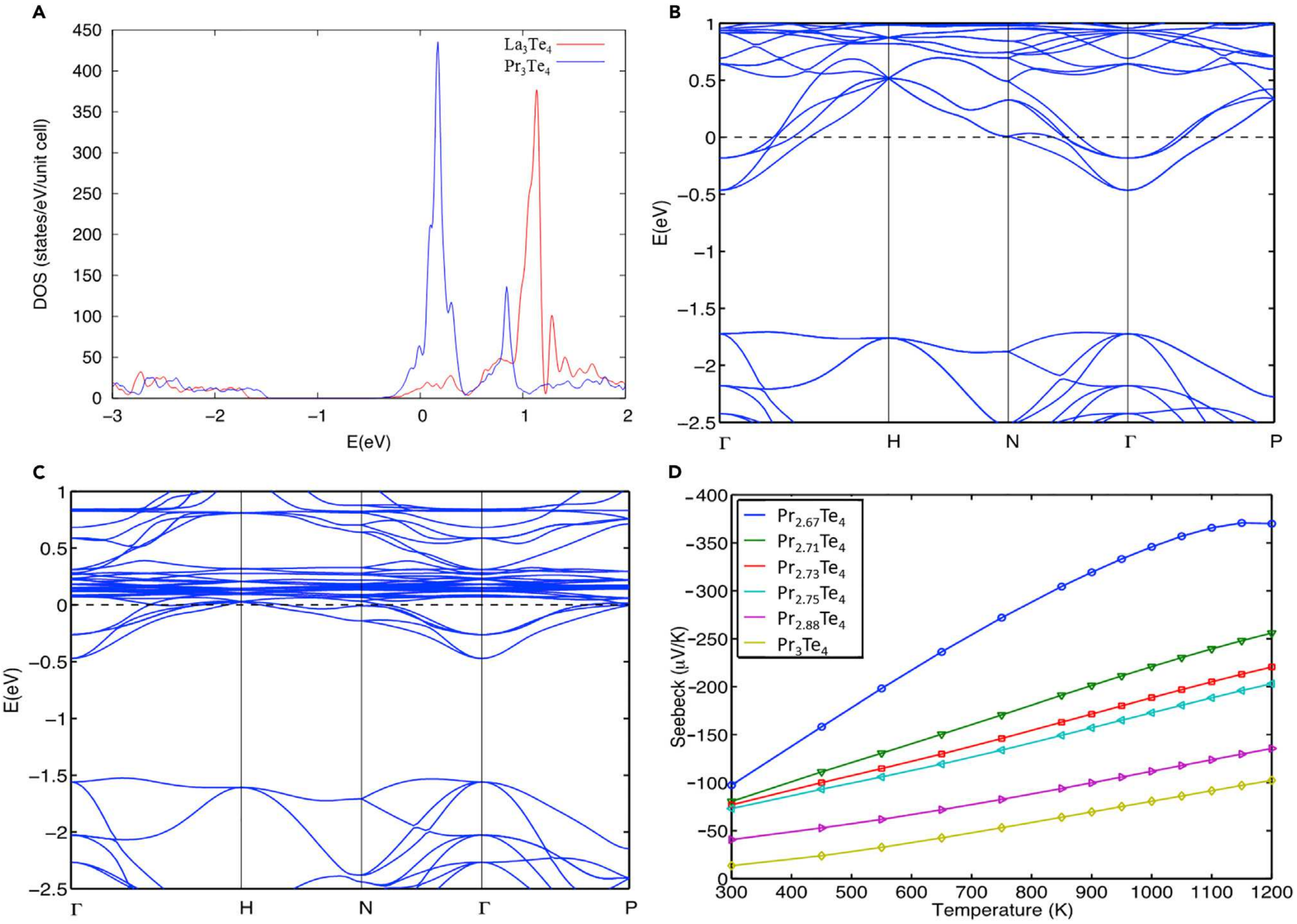

Figure 1. Calculated Electronic Band Structure of Pr_3Te_4 and La_3Te_4

(A) Comparison of density of states (DOS) of La_3Te_4 and Pr_3Te_4. The Fermi level is defined as $E_f = 0$ for both compounds.

(B) Calculated electronic band structure diagram of La_3Te_4.

(C) Calculated electronic band structure diagram of Pr_3Te_4.

(D) Seebeck coefficient of Pr_3Te_4 as a function of temperature and rare-earth vacancy concentration.

atoms include three *4f* valence electrons in the valence shell. This addition of *f* electrons has given Pr-containing compounds novel optical, magnetic, and superconducting properties.[23–25] While the electronic properties of $Pr_{3-x}Te_4$ have been previously reported, the use of melt synthesis led to inconsistencies in reported values.[4,26,27] To avoid these issues, we employed mechanochemical synthesis to produce $Pr_{3-x}Te_4$ samples with increasing vacancy concentrations and measured the thermoelectric properties.

RESULTS AND DISCUSSION

Pr_3Te_4 Electronic Structure

Band engineering is one of the key tools for optimizing *ZT* of complex materials. An important difference between Pr_3Te_4 and La_3Te_4 is the presence of three additional *f* electrons in Pr. We have studied the band structures and DOS of these two materials to understand the extent to which the *f* states affect the thermoelectric properties. Figure 1A compares the DOS of La_3Te_4 and Pr_3Te_4. The sharp peaks observed in the DOS of both compounds are mainly associated with the *f* orbitals (see discussion in the next paragraph). While the *f* peak in La_3Te_4 is located far above the Fermi level, the *f* peak in Pr_3Te_4

is situated near and at the Fermi level, resulting in a higher DOS in the energy range of interest to n-type thermoelectric materials. This enhancement in DOS at the Fermi level is one of the important requirements for improving transport properties. To have an enhanced transport property, the Fermi energy for the experimental value of the electron density should be close enough to the resonance in the DOS such that band contributions to *ZT* become dominant. An example of this observation can be found for the case of Ce_3Te_4, where the *f* peak is too far from the Fermi level to significantly contribute to the Seebeck coefficient at practical experimental conditions.[20]

The role of *f* electrons on the electronic properties can be further investigated by comparing partial DOS of La_3Te_4 and Pr_3Te_4. As seen from Figures S1 and S2, the main contribution to the DOS peak in the La_3Te_4 and Pr_3Te_4 comes from *5d* and *4f* orbitals of La and Pr, respectively. However, because the La *4f* peak in La_3Te_4 is located far from the Fermi level, significant contribution to the DOS and, thus, transport property at and near the Fermi level relies mostly on La *5d* orbitals for La_3Te_4. On the other hand, although the two peaks (the large and small ones) observed in Pr_3Te_4 DOS are also mainly contributed by the *f* orbitals and *d* orbitals, the contribution from the *f* orbitals dominates at the Fermi level. Consequently, for Pr_3Te_4 it is expected that the presence of three *f* electrons in Pr atoms would enhance the transport properties, compared with La atoms with no electrons in the *f* shells. In addition, Figures S1 and S2 also show a gap that separates the *f* peak from other lower energy states (with energy of less than ~1.4 eV) in both cases. The gap is ~0.91eV for Pr_3Te_4, which is smaller than that of La_3Te_4 (~1.01 eV). While the main contribution to the DOS peak is the *4f* orbitals, far below the Fermi level in the valence band at the energy of ~1.4 eV, Te *5p* orbitals are found to contribute the most to the DOS.

To acquire further insight into the difference in electronic properties of La_3Te_4 and Pr_3Te_4, we examined the band structures of both compounds. Figures 1B and 1C show the band structures of La_3Te_4 and Pr_3Te_4. Slightly above the Fermi level in the band structure of Pr_3Te_4 a denser region of flat bands is observed, which originates from the *4f* orbitals of Pr atoms. Further above the Fermi level (~0.5 eV), significant changes in the band structure are also observed for the case of Pr_3Te_4, especially at the H, N, and Γ points. The bands become flatter, and band degeneracy is changed dramatically. Due to the effect of *f* orbitals, the bands at the Γ point have smaller curvatures for the Pr_3Te_4 case than for La_3Te_4. Consequently, the effective masses are expected to be larger for Pr_3Te_4 than for La_3Te_4.

The Seebeck coefficients for Pr_3Te_4 and La_3Te_4 are computed using standard expressions derived from the linearized Boltzmann Transport Equation and the rigid band approximation to describe the variation of electron concentration due to vacancies.[19,28,29] In the rigid band approximation, the band structure of the studied compounds is assumed to be unchanged when varying the electron concentration; only the position of the Fermi energy is adjusted. Figure 1D presents the Seebeck coefficients of Pr_3Te_4 as a function of temperature and carrier concentration. Here the Seebeck coefficient increases with increasing temperature, and decreases with increasing carrier concentration. Figure S3 compares the Seebeck coefficient of both compounds. The plot shows larger Seebeck coefficients for Pr_3Te_4 than for La_3Te_4 for all carrier concentrations of interest (10^{20}–10^{22} cm^{-3}). The results are consistent with the increase in DOS due to the presence of *f* electrons observed near and at Fermi energy.

Sample Characterization

Densified, sintered compacts were ground using a mortar and pestle and their phase purities analyzed using powder X-ray diffraction (XRD). The diffraction pattern shown

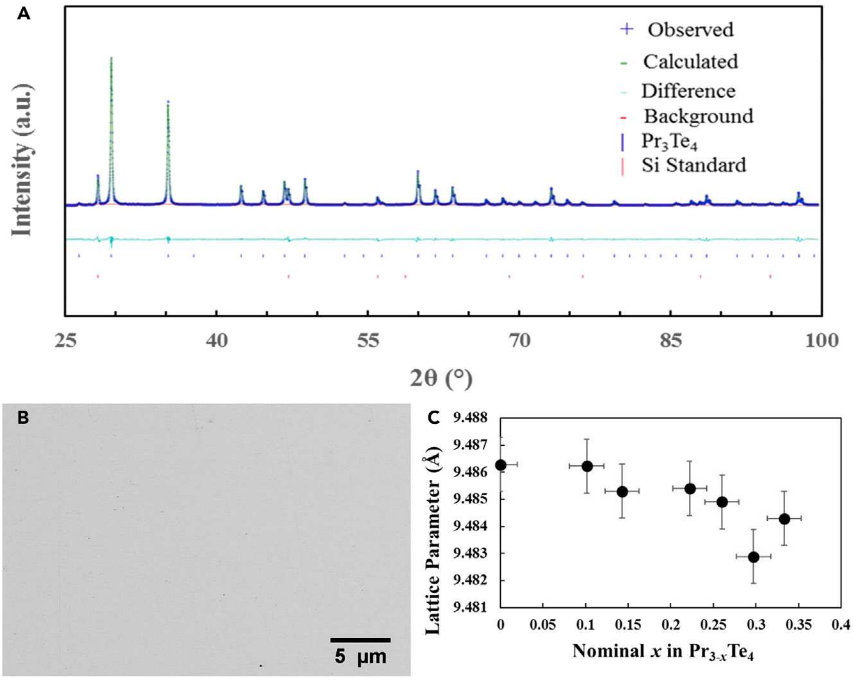

Figure 2. Phase and Compositional Analysis of $Pr_{3-x}Te_4$ Samples

(A) X-ray diffraction pattern of $Pr_{2.74}Te_4$ mixed with a Si internal standard. The pattern is representative of the diffraction patterns of other $Pr_{3-x}Te_4$ samples in this study, with no secondary or oxide phases present. Rietveld refinement was performed and the calculated pattern and difference curve are shown. The fit from the Rietveld analysis is in agreement with the Pr_3Te_4 phase. The goodness of fit was found to be 2.39 and $wR = 0.770\%$.

(B) BSE micrograph of the polished surface of the $Pr_{2.74}Te_4$ sample. The uniformity of the image contrast reflects the homogeneity of the samples. Dark regions in the image are from the small amount of residual porosity present in the sample.

(C) Lattice parameter calculated from Rietveld analysis as a function of vacancy concentration. Error bars in lattice parameters represent the diffractometer limit of ±0.001 Å and error bars in x represent 5%.

in Figure 2A is of a representative sample. No secondary or oxide phases were detected, and the pattern correlated with the Pr_3Te_4 pattern previously reported.[28] Phase homogeneity of the samples further verified by the backscattered electrons (BSE) on samples consolidated by spark plasma sintering (SPS) as shown in Figure 2B is typical of all samples, and the uniform contrast reflects the phase homogeneity of the sample. The dark areas in Figure 2B resulted from trace amounts of residual porosity in the sample. From Figure 2B, the porosity was calculated to be approximately 2.5%.

To determine the composition of each sample, we employed both wavelength dispersive X-ray spectroscopy (WDS) (on sintered samples) and Rietveld analysis (on ground compacts). These values were compared with nominal compositions in Table 1. Ten WDS measurements were averaged for each value given. WDS and nominal compositions were in good agreement for all compositions, as were the values calculated from Rietveld for samples near the compositions Pr_3Te_4 and $Pr_{2.67}Te_4$. The Rietveld calculations were found to underestimate the vacancy concentrations for intermediate compositions due to the XRD scan quality not having the necessary resolution for consistent calculation of the fractional occupancy, although the values are in good agreement with the nominal compositions. The lattice parameter for each sample was also determined from Rietveld analysis, as shown in Figure 2C. There was little change in the lattice parameter when the maximum number of vacancies was introduced, which

Table 1. Nominal Sample Composition Compared with Compositions Measured from WDS and Rietveld Analysis

Nominal Composition	WDS Composition	Rietveld Composition
Pr_3Te_4	$Pr_{3.03}Te_4$	$Pr_{2.97}Te_4$
$Pr_{2.90}Te_4$	$Pr_{2.93}Te_4$	$Pr_{2.92}Te_4$
$Pr_{2.86}Te_4$	$Pr_{2.86}Te_4$	$Pr_{2.91}Te_4$
$Pr_{2.78}Te_4$	$Pr_{2.78}Te_4$	$Pr_{2.86}Te_4$
$Pr_{2.74}Te_4$	$Pr_{2.78}Te_4$	$Pr_{2.79}Te_4$
$Pr_{2.70}Te_4$	$Pr_{2.70}Te_4$	$Pr_{2.68}Te_4$
$Pr_{2.67}Te_4$	$Pr_{2.61}Te_4$	$Pr_{2.67}Te_4$

The nominal and WDS compositions were in good agreement with one another. Compositions calculated via Rietveld analysis were in good agreement with nominal and WDS compositions for samples near Pr_3Te_4 and $Pr_{2.667}Te_4$, but samples with intermediate compositions were found to underestimate the vacancy concentrations.

is consistent with prior structural investigations of $Pr_{3-x}Te_4$.[28,29] The small change in lattice parameter is also observed in $La_{3-x}Te_4$; however, the mass density of $La_{3-x}Te_4$ is constant at 6.58 g cm^{-3} whereas that of $Pr_{3-x}Te_4$ is 7.27 g cm^{-3} when $x = 0$ and 6.91 g cm^{-3} when $x = 0.33$.[19,30–32] The difference in the density behavior as a function or rare-earth atomic vacancies for these two materials is not well understood and warrants further investigation.

Electronic Transport Properties

Electrical resistivity as a function of temperature was measured, and is shown in Figure 3A along with values previously reported for $La_{3-x}Te_{4.}$[19] All samples exhibited behavior expected for a degenerately doped semiconductor. The resistivity of the samples increased with increasing vacancy concentration due to the reduction in carrier concentration. Measurements made on samples with $x =$ 0.33 were conducted but the high resistivity of the samples presented difficulties in making ohmic contacts, which resulted in inaccurate Van der Pauw resistivity values. The resistivity of $Pr_{3-x}Te_4$ samples trends well with the values of $La_{3-x}Te_4$ for lower vacancy concentrations. However, at higher vacancy concentrations the $Pr_{3-x}Te_4$ samples exhibited higher resistivity values than $La_{3-x}Te_4$ with equivalent vacancy concentrations.

The temperature-dependent Seebeck coefficient is shown in Figure 3B. The Seebeck coefficient increased with increasing vacancy due to the reduction in carrier concentration, as expected. Similar to what was observed with the high-temperature resistivity, the $Pr_{3-x}Te_4$ samples with lower vacancy concentrations were found to be similar to those of $La_{3-x}Te_4$, and at higher vacancy concentrations the $Pr_{3-x}Te_4$ samples yielded higher Seebeck coefficients compared with $La_{3-x}Te_4$. Specifically, the $Pr_{2.74}Te_4$ composition exhibited a 25% increase in the Seebeck coefficient when compared with $La_{2.74}Te_4$. The improved Seebeck coefficient of $Pr_{2.74}Te_4$ resulted in an increased power factor (σS^2) over $La_{2.74}Te_4$ (Figure 3C).

An effective mass of $m^* = 3.5m_e$ and $2.13m_e$ were calculated for $Pr_{2.74}Te_4$ and $La_{2.74}Te_4$, respectively, using a single parabolic band model (Figure S8). An effective mass of $2.13m_e$ matches well with previously reported values for $La_{3-x}Te_4$, which range from $1.6m_e$ to $2.75m_e$.[4,7,9] The increased effective mass of $Pr_{2.74}Te_4$ over $La_{2.74}Te_4$ is consistent with the observed increase in the Seebeck coefficient at equivalent vacancy concentrations, and supports the hypothesis that the *4f* electrons modified the band structure favorably over $La_{3-x}Te_4$.

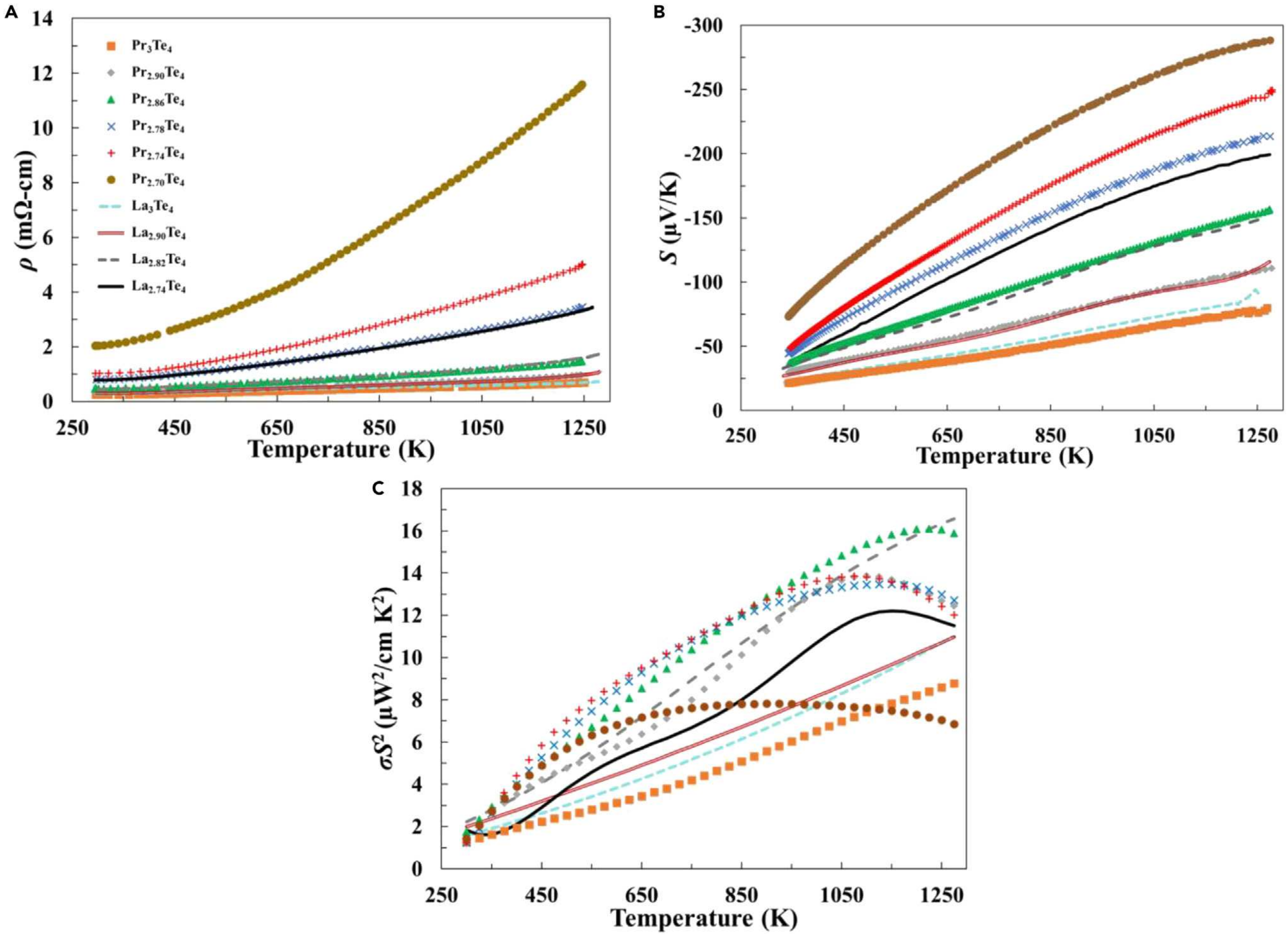

Figure 3. High-Temperature Electronic Properties of $Pr_{3-x}Te_4$ Samples

(A) Temperature-dependent resistivity of $Pr_{3-x}Te_4$ samples compared with that of $La_{3-x}Te_4$.[7] The samples are indicated by their nominal compositions. The higher vacancy concentration $Pr_{3-x}Te_4$ samples had resistivities much higher than equivalently vacancy doped $La_{3-x}Te_4$.

(B) Seebeck coefficient as a function of temperature of $Pr_{3-x}Te_4$ samples compared with that of $La_{3-x}Te_4$.[7] $Pr_{3-x}Te_4$ samples at higher vacancy concentrations exhibited significantly larger Seebeck values compared with $La_{3-x}Te_4$.

(C) Temperature-dependent power factor (σS^2) of $Pr_{3-x}Te_4$ and $La_{3-x}Te_4$ samples. An increase was observed for $Pr_{2.74}Te_4$ over $La_{2.74}Te_4$ across the temperature range measured.

Thermal Transport Properties

The total thermal conductivity is shown in Figure 4A and was calculated from $\kappa = DC_pd$, where D is the measured thermal diffusivity, C_p is the measured heat capacity (Figure S9), and d is the sample density (Table S2). Thermal conductivities were found to range from 5 to 35 mW cm^{-1} K^{-1}, with the thermal conductivity decreasing with increasing vacancy concentration. This was expected, as the total thermal conductivity is composed of two components, the electronic and lattice thermal conductivities, and is given by $\kappa = \kappa_e + \kappa_L$. Therefore the increased vacancy concentration had a reduced electronic term from the corresponding decreased carrier concentration. This behavior is similar to that previously reported for $La_{3-x}Te_4$.

When samples with equivalent vacancy concentrations were compared, it was found that $Pr_{3-x}Te_4$ samples exhibited a significantly lower thermal conductivity than $La_{3-x}Te_4$. To determine whether this decrease was due to a change in the electronic or lattice contributions, we calculated the lattice thermal contribution. The lattice

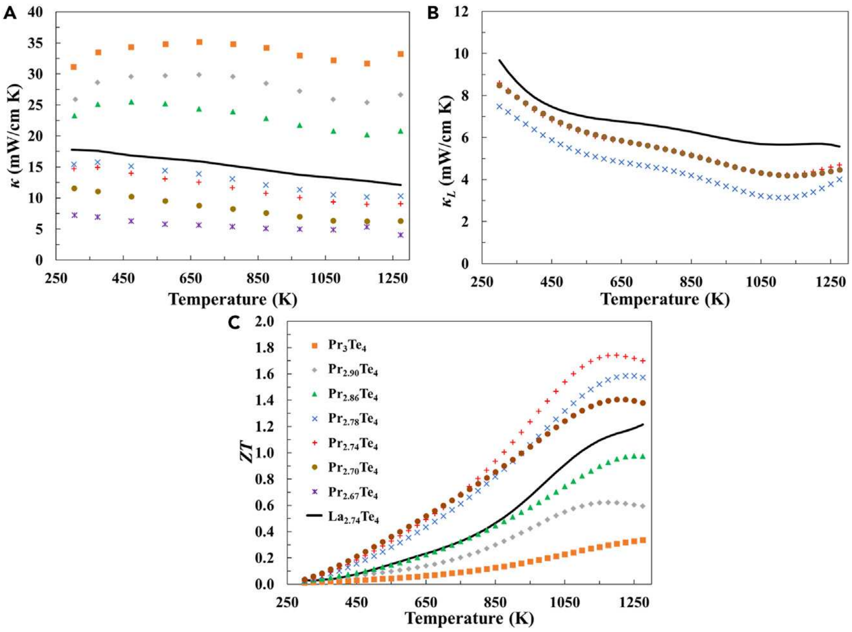

Figure 4. Temperature-Dependent Thermal Conductivity and Dimensionless Figure of Merit of $Pr_{3-x}Te_4$

(A) Total thermal conductivities of $Pr_{3-x}Te_4$ compared with $La_{2.74}Te_4$.[7]

(B) Lattice thermal conductivities calculated using the Wiedemann-Franz law. $Pr_{3-x}Te_4$ samples with higher carrier concentrations were omitted due to strong deviation from the Wiedemann-Franz law.

(C) Temperature-dependent thermoelectric figure of merit, ZT, as a function of temperature. The optimized ZT for $La_{3-x}Te_4$ is shown for comparison. The error in ZT is approximately 30%.[7]

thermal conductivity was found by first calculating the electronic contribution using the Wiedemann-Franz law $\kappa_e = L\sigma T$, where L is the Lorenz number and σ is the electrical conductivity; the electronic contribution was then subtracted from the total thermal conductivity. A simplified variable Lorenz number was used, which was calculated as a function of Seebeck coefficient using the approximation $L = 1.5 + \exp(-|S|/116)$ and resulted in Lorenz numbers between 1.5 and 2.2 × 10^{21} WΩ K^{-2}.[33]

Figure 4B shows the calculated lattice contributions to the total thermal conductivity, κ_L, for vacancy concentrations similar to $La_{2.74}Te_4$. The intrinsically low κ_L resulted from the complexity of the Th_3P_4, which promoted substantial Umklapp scattering of acoustic phonons.[22] κ_L values for the $Pr_{3-x}Te_4$ samples were found to be similar to one another and lower than that calculated for $La_{2.74}Te_4$ from room temperature to 1,275 K. To investigate the origin of the reduced κ_L in $Pr_{3-x}Te_4$, we measured the elastic moduli and sound velocities of both $La_{2.74}Te_4$ and $Pr_{2.74}Te_4$ from room temperature up to 573 K. The elastic moduli $Pr_{2.74}Te_4$ was found to be slightly lower than $La_{2.74}Te_4$. Combined with the higher density of $Pr_{2.74}Te_4$, this led to a small decrease in the speed of sound (Figure S4), which is consistent with the lower κ_L.

Thermoelectric Figure of Merit

Combining the electronic and thermal transport properties, the ZT was calculated as a function of temperature (Figure 4C), with a propagated error of 30%. ZT was found to increase with increasing vacancy concentration until $x = 0.26$ and then began to decrease. A peak ZT of 1.7 at 1,200 K was achieved. This represents a 50%

improvement over the optimized ZT of 1.1 reported for $La_{3-x}Te_4$.[7] The improvement in ZT resulted from the large increase in the Seebeck coefficient from the electronic states introduced by the 4*f* electron in addition to the lower thermal conductivity, which resulted from a decreased lattice contribution.

Conclusion

Density functional theory was used to calculate the DOS and energy band diagram for Pr_3Te_4. It was found that the 4*f* electrons of Pr cause a sharp increase in the DOS near the conduction band edge when compared with $La_{3-x}Te_4$. The increase in the DOS was predicted to improve the Seebeck coefficient of *n*-type $Pr_{3-x}Te_4$. A series of $Pr_{3-x}Te_4$ samples with varying vacancy concentrations were successfully synthesized using mechanochemical methods. The stoichiometry and phase purity were analyzed through a combination of WDS and XRD. The electronic and thermal properties were measured and $Pr_{3-x}Te_4$ exhibited a 25% improvement in the Seebeck coefficient over $La_{3-x}Te_4$ near optimal vacancy concentration levels. Additionally, $Pr_{3-x}Te_4$ was found to have decreased thermal conductivity due to a smaller lattice contribution than $La_{3-x}Te_4$. The increased Seebeck coefficient and reduced thermal conductivity resulted in a peak ZT of 1.7 at 1,200 K. The successful theoretical prediction and experimental verification of the modified band structure of $Pr_{3-x}Te_4$ due to the *4f* electrons suggests that further improvements can be made by incorporating other rare-earth elements.

EXPERIMENTAL PROCEDURES

Synthesis

A mechanochemical approach was used to synthesize samples of the desired stoichiometry. Elemental Pr (99.9%, Stanford Materials) and Te shot (99.999, 5N Plus) were combined and sealed under argon in stainless-steel ball mill vials with stainless-steel balls. They were then milled (SPEX SamplePrep 8000) for over 10 hr until homogeneous black powders of $Pr_{3-x}Te_4$ were produced. The powders were then densified in graphite dies through SPS at a pressure of 80 MPa and at temperatures above 1,200°C for 30 min under vacuum. The Archimedes method was used to measure density, and the compacted samples were found to be 97% dense or greater of theoretical values (Table S2).

Characterization

XRD data were collected with a Phillips PANalytical X'Pert Pro diffractometer using Cu Kα radiation. Compacted samples were ground using a mortar and pestle and then mixed with Si powder (−325 mesh, 99.999%, Alfa Aesar) to use as an internal standard during Rietveld analysis. Due to the $Pr_{3-x}Te_4$ powders being highly air sensitive, the powders were sealed with 1-mm thick Kapton film on an Si zero background holder under argon. Scans were performed over a 2θ range of 25°–100°, with a 0.02° step size and a time of 11.5 s per step. Rietveld refinement was done using GSAS-II crystallographic data analysis software.[34] Structural data for the cubic phase with space group $I\bar{4}3d$ from Mitarov et al. was used for refinement.[30] To perform a stable refinement of the Pr occupancy, the occupancy on the Te position was held at 100% as no vacancies were expected.

WDS was performed to assess the elemental compositions of the sintered compacts. A JEOL JXA-8200 electron probe microanalyzer was utilized, with $PrPO_4$ and elemental Te as the standards. Ten points were measured for each sample and the elemental compositions were averaged to determine the composition of the samples. Backscattered electron scanning electron microscopy images were taken on a Zeiss 1550 VP scanning electron microscope.

A custom-built combined 4-point probe and Hall effect system was used to measure the electrical resistivity and Hall voltage, from which the carrier concentration and mobility were calculated.[35] The Seebeck coefficient was measured using a custom-fabricated instrument.[36] Thermal diffusivity was measured using a commercial Netzsch LFA 457 system and specific heat capacity was measured using a Netzsch DSC 404. The thermal conductivity was calculated by $\kappa = DC_pd$, where κ is the thermal conductivity, D is the thermal diffusivity, C_p is the specific heat capacity, and d is the sample density. Errors in electrical resistivity, Seebeck, and thermal conductivity were found to be approximately 5%, 20%, and 10%, respectively. The measured properties of the samples were not found to change with repeated thermal cycling, indicating high stability for the rare-earth vacancies.

High-temperature resonant ultrasound spectroscopy (RUS) measurements from 300 K to 573 K (300°C) were performed on bulk samples using a Magnaflux-RUS Quasar 4000 system under flowing argon to minimize oxidation with a frequency range of 0–500 kHz with 16.67-Hz step size. Data were analyzed using the Quasar2000 ClyModel software package.

DFT Calculations

The structural relaxation and electronic properties of La_3Te_4 and Pr_3Te_4 were computed with the open-source DFT software package Quantum Espresso.[37] It is well known that the *f* states in rare-earth compounds are not adequately described by standard local density approximation (LDA) and generalized-gradient approximation due to strong electronic correlation effects.[38,39] To address this shortcoming, PBE plus on-site Coulomb interaction (PBE + U) was used in this work.[40–42] The on-site Coulomb interaction serves to correct the self-interaction for the *f* electrons localized at the rare-earth sites. Projected augmented wave (PAW) potentials generated with the AUTOPAW program were used for La and Pr with an energy cutoff of 60 Ry for the wave functions and a charge density cutoff of 540 Ry.[43,44] Since Pr_3Te_4 and La_3Te_4 are metallic, the Mazari-Vanderbilt smearing scheme was used to expedite the convergence toward self-consistency.[45] Brillouin zone k-point sampling of 13 × 13 × 13 and 17 × 17 × 17 were used for the structural relaxation and transport property calculations (Seebeck coefficient), respectively. The choice of energy cutoff and k points was derived from the details of convergence tests.

La_3Te_4 and Pr_3Te_4 have the Th_3P_4 structure, belonging to the cubic crystal system and space group $I\bar{4}3d$.[4,7] The atomic positions of both structures were relaxed for various fixed lattice parameters. The lattice parameter corresponding to the minimum total energy is found to be 9.70 Å for La_3Te_4, in good agreement with the experimental values of 9.622 Å.[7] For Pr_3Te_4, we computed the lattice constant for several values of U. We found that $U = 4.0$ eV gives a relaxed lattice constant of 9.50 Å, in excellent agreement with the experimental value of 9.482 Å, with an error of ~0.2%.[30] At room or higher temperatures, both materials are paramagnetic. For this reason, we discuss the electronic properties of Pr_3Te_4 for non-spin polarized calculations, since it more closely describes the properties of Pr_3Te_4 at or above room temperature.

SUPPLEMENTAL INFORMATION

Supplemental Information includes nine figures and two tables and can be found with this article online at https://doi.org/10.1016/j.joule.2018.01.013.

ACKNOWLEDGMENTS

This work was performed at the California Institute of Technology/Jet Propulsion Laboratory under contract with the National Aeronautics and Space Administration. This work was supported by the NASA Science Missions Directorate under the Radioisotope Power Systems Program's Thermoelectric Technology Development Project.

AUTHOR CONTRIBUTIONS

Conceptualization, D.C., B.S.D., J.-P.F., and S.K.B.; Investigation, D.C., B.E.H., T.V., P.V.A., K.L., and D.S.; Formal Analysis, D.C., B.E.H., T.V., D.M.S., and A.Z.; Resources, A.Z., J.-P.F., and S.K.B.; Writing – Original Draft, D.C. and A.Z.; Writing – Review & Editing, K.L., D.M.S., A.Z., and S.K.B.; Supervision, B.S.D., J.-P.F., and S.K.B.; Funding Acquisition, J.-P.F. and S.K.B.

DECLARATION OF INTERESTS

The authors declare no competing interests.

Received: October 30, 2017
Revised: December 14, 2017
Accepted: January 26, 2018
Published: February 19, 2018

REFERENCES

1. Rowe, D.M. (1995). CRC Handbook of Thermoelectric Materials (CRC Press).
2. Yang, J., and Caillat, T. (2006). Thermoelectric materials for space and automotive power generation. MRS Bull. *31*, 224–229.
3. Fleurial, J.-P. (2009). Thermoelectric power generation materials: technology and application opportunities. JOM *61*, 74–85.
4. Wood, C. (1988). Materials for thermoelectric energy conversion. Rep. Prog. Phys. *51*, 459–539.
5. Vining, C.B., and Fleurial, J.-P. (1993). Silicon-Germanium: An Overview of Recent Development (AIP Press), pp. 87–120.
6. Snyder, G.J., and Toberer, E.S. (2008). Complex thermoelectric materials. Nat. Mater. *7*, 105–114.
7. May, A.F., Fleurial, J.-P., and Snyder, G.J. (2008). Thermoelectric performance of lanthanum telluride produced via mechanical alloying. Phys. Rev. B *78*, 125205.
8. Cutler, M., Leavy, J.F., and Fitzpatrick, R.L. (1964). Electronic transport in semimetallic cerium sulfide. Phys. Rev. *133*, A1143.
9. Cutler, M., and Leavy, J.F. (1964). Electronic transport in high-resistivity cerium sulfide. Phys. Rev. *133*, A1153.
10. Cutler, M., Fitzpatrick, R.L., and Leavy, J.F. (1963). The conduction band of cerium sulfide Ce$_{3-x}$S$_4$. J. Phys. Chem. Solid. *24*, 319–327.
11. Zhuze, P., Sergeeva, V.M., and Golikova, O.A. (1970). Kinetic processes in rare-earth chalcogenides having the composition Ln $_3$X$_4$. Sov. Phys. Solid State *11*, 2071.
12. Gadzhiev, G., Ismailov, S.M., Abdullaev, K.K., Khamidov, M.M., and Omarov, Z.M. (2001). Thermal and electrical properties of gadolinium sulfides at high temperatures. High Temp. *39*, 407–412.
13. Taher, S.M., and Gruber, J.B. (2001). Thermoelectric efficiency of rare earth sesquisulfides. Mat. Res. Bull. *16*, 1407–1412.
14. Vickerv, R.C., and Muir, H.M. (1961). Thermoelectric properties of rare earth chalcogenides. Adv. Energy Convers. *1*, 179–186.
15. Wood, C., Lockwood, A., Parker, J., Zoltan, A., Zoltan, D., Danielson, L.R., and Raag, V. (1985). Thermoelectric properties of lanthanum sulfide. J. Appl. Phys. *58*, 1542–1547.
16. Danielson, L.R., Raag, V., and Wood, C. (1985). Thermoelectric properties of rare earth chalcogenides. Intersociety Adv. Energy Convers. Eng. Conf. Proc. *3*, 3.531–3.535.
17. Eliseev, A.A., Yarembash, E.I., Kuznetsov, Y.G., Vigileva, E.S., Reshchikova, A.A., and Anotonoa, L.I. (1964). Telluridy lantana. Russ. J. Inorg. Chem. *9*, 876–881.
18. Ramsey, T.H., Steinfink, H., and Weiss, E.J. (1965). The phase equilibria and crystal chemistry of the rare earth-group VI systems. IV. Lanthanum-tellurium. Inorg. Chem. *4*, 1154–1157.
19. May, A.F., Singh, D.J., and Snyder, G.J. (2009). Influence of band structure on the large thermoelectric performance of lanthanum telluride. Phys. Rev. B *9*, 153101.
20. Vo, T., von Allmen, P., Huang, C.-H., Ma, J.M., Bux, S.K., and Fleurial, J.-P. (2014). Electronic and thermoelectric properties of Ce$_3$Te$_4$ and La$_3$Te$_4$ computed with density functional theory with on-site Coulomb interaction correction. J. Appl. Phys. *116*, 133701.
21. May, A.F., Fleurial, J.-P., and Snyder, G.J. (2010). Thermoelectric performance of lanthanum telluride produced via mechanical alloying. Chem. Mater. *22*, 2995–2999.
22. Ma, J.M., Clarke, S.M., Zeier, W.G., Vo, T., von Allmen, P., Snyder, G.J., Kaner, R.B., Fleurial, J.-P., and Bux, S.K. (2015). Mechanochemical synthesis and high temperature thermoelectric properties of calcium-doped lanthanum telluride La$_{3-x}$Ca$_x$Te$_4$. J. Mater. Chem. C *3*, 10459–10466.
23. Weber, M.J. (1979). Methods of Experimental Physics (Academic Press), Chp. 3.
24. Wu, W., Xuan, Y., Yin, J.N., and Xie, J. (2015). Influence of praseodymium doping concentration on the structural and optical properties of strontium molybdate crystals. Res. Chem. Inter. *41*, 2479–2488.
25. Lamberti, V.E., Rodriguez, M.A., Trybulski, J.D., and Navrotsky, A. (1996). Praseodymium and high-temperature superconductivity: thermodynamic, structural, and critical correlations. J. Mater. Res. *11*, 1061–1064.
26. Gschneidner, K.A., Nakahara, J.F., Beaudry, B.J., and Takeshita, T. (1987). Lanthanide refractory semiconductors based on the Th3P$_4$ structure. Mat. Res. Soc. Symp. Proc. *97*, 359–370.
27. Golikovai, O.A., Rudnikv, M., Sergeeva, M., Kazanin, M.M., and Tkalenko, E.N. (1976). On the conductivity of rare-earth metal chalcogenides Ln$_{3-x}$X$_4$ ($0 < x < 0.33$). Phys. Status Solidi A *37*, 199–203.

28. Ascroft, N.W., and Mermin, N.D. (1976). Solid State Physics (Harcourt College Publisher).

29. Mott, N.F., and Jones, H. (1936). The Theory of the Properties of Metals and Alloys (The Clarendon Press).

30. Mitarov, R.G., Tikhonov, V.V., Vasil'ev, L.N., Golubkov, A.V., and Smirnov, I.A. (1975). Specific heat of Pr_3Te_4 and La_3Te_4. Phys. Status Solidi A *30*, 496–500.

31. Yarembash, E.I., Eliseev, A.A., Vigileva, E.S., and Antonova, L.I. (1967). X-ray study of praseodymium tellurides. Inorg. Chem. *3*, 2184–2189.

32. Cox, W.L., Steinfink, H., and Bradley, W.F. (1966). The structure refinement of La_2Te_3, a Th_3P_4 type structure. Inorg. Chem. *5*, 318–319.

33. Kim, H.S., Gibbs, Z.M., Tang, Y., Wang, H., and Snyder, G.J. (2015). Characterization of Lorenz number with Seebeck coefficient measurement. APL Mater. *3*, 041506.

34. Toby, B.H., and Von Dreele, R.B. (2013). GSAS-II: the genesis of a modern open-source all purpose crystallography software package. J. App. Cryst. *46*, 544–549.

35. Borup, K.A., Toberer, E.S., Zoltan, L.D., Nakatsukasa, G., Errico, M., Fleurial, J.-P., Iversen, B.B., and Snyder, G.J. (2012). Measurement of the electrical resistivity and Hall coefficient at high temperatures. Rev. Sci. Instr. *83*, 123902.

36. Wood, C., Zoltan, D., and Stapfer, G. (1985). Measurement of Seebeck coefficient using a light pulse. Rev. Sci. Instr. *56*, 719–722.

37. Giannozzi, P., Baroni, S., Bonini, N., Calandra, M., Car, R., Cavazzoni, C., Ceresoli, D., Chiarotti, G.L., Cococcioni, M., Dabo, I., et al. (2009). QUANTUM ESPRESSO: a modular and open-source software project for quantum simulations of materials. J Phys Condens Matter. *21*, 395502.

38. Kohn, W., and Sham, L.J. (1965). Self-consistent equations including exchange and correlation effects. Phys. Rev. *140*, A1133.

39. Perdew, J.P., Burke, K., and Ernzerhof, M. (1996). Generalized gradient approximation made simple. Phys. Rev. Lett. *77*, 3865.

40. Anisimov, V.I., Zaanen, J., and Andersen, O.K. (1991). Band theory and Mott insulators: Hubbard U instead of Stoner I. Phys. Rev. B *44*, 943.

41. Anisimov, V.I., Solovyev, I.V., Korotin, M.A., Czyżyk, M.T., and Sawatzky, G.A. (1993). Density-functional theory and NiO photoemission spectra. Phys. Rev. B *48*, 16929.

42. Cococcioni, M., and De Gironcoli, S. (2005). Linear response approach to the calculation of the effective interaction parameters in the LDA+ U method. Phys. Rev. B *71*, 035105.

43. Holzwarth, N.A.W., Tackett, A.R., and Matthews, G.E. (2001). A Projector Augmented Wave (PAW) code for electronic structure calculations, Part I: atompaw for generating atom-centered functions. Comput. Phys. Comm. *135*, 329–347.

44. Tackett, A.R., Holzwarth, N.A.W., and Matthews, G.E. (2001). A Projector Augmented Wave (PAW) code for electronic structure calculations, Part II: pwpaw for periodic solids in a plane wave basis. Comput. Phys. Comm. *135*, 348–376.

45. Marzari, N., Vanderbilt, D., De Vita, A., and Payne, M.C. (1999). Thermal contraction and disordering of the Al (110) surface. Phys. Rev. Lett. *82*, 3296.